# Effect of Shape and Size on the Transport of Floating Particles on the Free-surface of a Meandering Stream

**Henri R. Sanness Salmon**[1], **Lucia J. Baker**[2], **Jessica L. Kozarek**[3], **Filippo Coletti**[1]

[1]Department of Mechanical and Process Engineering, Swiss Federal Institute of Technology (ETH), CH-8092 Zürich, Switzerland
[2]Department of Mechanical Engineering, University of Washington, Seattle, WA 98195, USA
[3]St. Anthony Falls Laboratory, University of Minnesota, Minneapolis, Minnesota, MN 55455, USA

**Key Points:**

- Velocity of particles floating on turbulent streams are weakly affected by their shape and size.
- Larger particles disperse faster on the free-surface due to their ability to filter out the small-scale turbulent fluctuations.
- Rods re-orient following the mean shear of the surface flow and rotate according to the integral scales of the free-surface turbulence.

Corresponding author: Henri R. Sanness Salmon, `rsanness@ethz.ch`

## Abstract

Understanding how floating particles are transported by streaming waters is crucial in predicting the transport of plastic pollution, which is dramatically abundant in rivers, lakes, and oceans. Using particle tracking velocimetry, we investigate the motion of floating particles of different shape and size on the turbulent free-surface of a field-scale meandering stream. We consider two locations with different turbulence levels where the role of surface waves on the transport is deemed negligible. Millimetre-sized spheres are used as tracers to characterise the surface flow. These are compared with centimetre-sized discs and rods, much larger than the tracers, approximating typical-sized pieces of litter found in rivers. These larger particles exhibit similar velocities as the small tracers but filter out the extreme accelerations. Consequently, their motion is more time-correlated and their spreading rate is larger. This notion is confirmed by the mean-square displacement of single particles and mean-square separation of particle pairs, which grow faster in time compared to the tracers. The rotation of the rods, affected by a range of turbulent scales, reduces the correlation time scale of their translational motion, and leads to a slower dispersion compared to the discs, despite the rods' length being larger than the discs' diameter. Taken together, these results indicate that the motion of finite-size objects floating on non-wavy turbulent water is consistent with the behaviour of inertial particles in three-dimensional turbulence. These results can be valuable when constructing predictive models of floating plastics in natural waters.



## Plain Language Summary

Plastic debris is a rising global issue severely affecting the state of our rivers, lakes and oceans. Understanding how pieces of litter, often floating, travel in streaming waters is crucial for predicting and ultimately limiting plastic pollution. The main goal of this research is to investigate how the shape and size of small floating objects may affect their journey on the surface of water. To this end, we use high-speed video recordings to track floating objects of different shape and size in an outdoor stream laboratory. The motion of centimetre-sized discs and rods, approximating typical pieces of plastics found in rivers, is directly compared to the motion of millimetre-sized spheres that follow the surface flow. We find that the larger discs and rods spread faster on the surface of water. Not only can these results be used to devise effective sequestration strategies, but they can be important to inform computer models that predict the abundance and fate of plastic litter in natural waters.


## 1 Introduction

Plastic debris is ubiquitous in our lakes, oceans, and coastal waters, posing serious threats to human health and the environment (Eriksen et al., 2013; van Sebille et al., 2015; Lebreton et al., 2018). Recent findings demonstrate that about 1,000 rivers account for 80 % of the global annual emissions of 0.8 to 2.7 million tons of plastics into the oceans per year, with small urban rivers among the most polluting (Meijer et al., 2021). Riverine ecosystems themselves are affected by such pollution (van Emmerik & Schwarz, 2020). Plastic objects enter such systems in a wide range of compositions, shapes, and sizes before degrading into so-called microplastics (typically defined as smaller than 5 mm). A large proportion of the plastic waste in the U.S. is comprised of polyethylene and polypropylene, which are less dense than fresh water (Jambeck et al., 2015). In general, it is estimated that more than half of all plastics produced are positively buoyant (Geyer et al., 2017). The question that motivates the present study is at which rate floating mesoplastics (particles in the size range of 5 to 50 mm) spread over the surface of turbulent streaming waters.

The transport of floating particles has been mainly investigated in terms of its dependence on surface waves. These impart a net drift velocity in the direction of wave propagation, known as Stokes drift (van den Bremer & Breivik, 2018). While this is typically much smaller than the mean advective velocity, its magnitude increases with wave steepness and it can play a role in the long-term dispersion (van Sebille et al., 2020). DiBenedetto et al. (2018, 2019) showed that non-spherical particles in wavy waters tend to follow a preferred orientation, which affects their settling velocity if those are negatively buoyant. For buoyant particles, DiBenedetto (2020) found that waves result in non-uniform particle concentration.

Here we focus on regimes and scales where surface waves do not appreciably modify the dispersion along the free-surface, which is instead dictated by turbulence. The nature of turbulence on the vicinity of the surface is still debated. Pan and Banerjee (1995) identified hallmark features such as upwelling and downwelling motions and long-lived vortices. Kumar et al. (1998) measured a $k^{-3}$ decay of the velocity spectra ($k$ being the wavenumber), consistent with the expectation for two-dimensional (2D) turbulence. On the other hand, the field measurements of Chickadel et al. (2011) displayed a $k^{-5/3}$ behaviour typical of three-dimensional (3D) turbulence. In the riverine environment, the shallowness of the flow plays a significant role in determining the nature of the turbulence: in particular, in the presence of strong lateral shear, the limited depth inhibits vortex stretching and may result in vortex dynamics akin to 2D-turbulence, especially at low wavenumbers (Uijttewaal & Booij, 2000). Most previous studies focused on free-surface turbulence have been concerned with the topological features of the flow, often in relation to air-water gas fluxes (Shen et al., 1999; Shen & Yue, 2001; McKenna & McGillis, 2004; Turney & Banerjee, 2013; Herlina & Wissink, 2014), with only few studies concerned with the transport of particles on it. Particularly, Cressman et al. (2004) and Lovecchio et al. (2013) found that tracer particles floating on the free-surface cluster into string-like structures with long lifetimes. Characteristic features of shallow flows, such as transitional macro-vortices, have been found to greatly affect the single-particle and particle-pair dispersion (Stocchino et al., 2011).

Several field studies have been concerned with natural free-surface flows, focusing on the effectiveness of free-surface velocity measurements, e.g., for discharge estimation as well as flow monitoring during flood events. The methods include acoustic Doppler velocimetry (ADV) but also imaging techniques originally developed for laboratory flow studies, such as particle image velocimetry (PIV) and particle tracking velocimetry (PTV) (Raffel et al., 2018; Adrian & Westerweel, 2011). Free-surface PIV and PTV present technical challenges even in laboratory studies, e.g., the choice of appropriate tracers and their successful imaging in spite of surface reflections (Weitbrecht et al., 2002; Miozzi et al., 2010; Miozzi & Romano, 2020; Gomit et al., 2022). The difficulties are exacerbated in field studies due to uneven natural illumination and scarcity of detectable floating tracers. Nevertheless, these techniques have gained favor in riverine flow investigations due to the richness of the data they can provide (Jin & Liao, 2019; Tauro et al., 2016, 2019).

Here we investigate experimentally the motion of floating particles on the turbulent free-surface of a meandering stream in an outdoor facility which offers laboratory-quality measurements and control in a field-scale setting. The main goal of the study is to explore the influence of the shape and size of floating particles along their trajectories when driven by the multi-scale fluctuations of the free-surface flow. The focus is on size ranges relevant to meso- and macroplastics ($> 5\,\mathrm{mm}$) which are highly relevant to but largely understudied in river flows (van Emmerik & Schwarz, 2020). Applying time-resolved PTV to millimetre-sized tracers, we obtain surface velocity fields at two different locations along the stream. We then characterize the transport of centimetre-sized discs and rods and directly compare them to the behaviour of the tracers. In particular, we examine the floating particles response to the free-surface turbulent fluctuations which in turn affects their spreading rate. The rotational dynamics of the rods are then considered to gain insight on their dispersion as compared to the discs. As we will discuss, the sensitivity of the particle dispersion to small-scale turbulence may have important consequences for modeling approaches based on flow velocity data (which are necessarily coarse-grained in space and time).

(a) (b)


**Figure 1.** (a) The OSL facility, with the locations of the two ROIs (Meander and Riffle) indicated by arrows. The tent, shown here at a downstream location, is deployed over the ROIs in the present experiments. (b) The traversing system holding the camera used for free-surface imaging, indicating the approximate location of the field of view in the Meander and the coordinate system.

# 2 Materials and Methods

## 2.1 Field-scale Stream Facility and Hydrodynamic Characterization

Measurements are performed in the Outdoor StreamLab (OSL), an outdoor field-scale stream facility at the Saint Anthony Falls Laboratory, University of Minnesota (Figure 1a). Water is drawn from the Mississippi River, flows through a meandering channel and discharges back into the river. The flow rate is controlled via a valve at the inlet, and the incoming water flows into a headbox and over a weir before entering the channel. A Massa M300 ultrasonic distance probe and a sonar transducer are mounted on a programmable measurement carriage, performing 2D elevation scans of the water surface and channel bed. The monitoring of the water height at the weir allows real time calculation of the flow rate $Q$. Two regimes are considered, $Q = 32.1\,\mathrm{L\,s^{-1}}$ and $Q = 53.7\,\mathrm{L\,s^{-1}}$, for which transport of sediment is negligible and the bed is static. Measurements are acquired in two regions of interest (ROIs): one located at one of the meanders in the stream, and the other at the straight section upstream of a riffle. We will refer to these measurement locations as the Meander and the Riffle, respectively.

The bathymetries of both ROIs are shown in Figure 2a-b. The origin of the global coordinate system is chosen to be on the bank of the Meander, with $x$ approximately in the streamwise direction, $y$ pointing from the inner to the outer bank, and $z = 0\,\mathrm{m}$ corresspionding to the water surface. At the Riffle we also define an additional coordinate system $x' - y'$, with $x'$ approximately aligned with the local flow direction.

The sub-surface flow velocity in the Meander is also characterized by a Nortek Vectrino ADV probe traversed along the cross-section at $x = 1\,\mathrm{m}$. The phase-space thresholding technique described in Parsheh et al. (2010) is used to remove occasional spurious velocity spikes due to air bubbles. Measurements are acquired at 100 Hz for 120 s, in 23 and 28 locations along the cross-section for $Q = 32.1\,\mathrm{L\,s^{-1}}$ and $Q = 53.7\,\mathrm{L\,s^{-1}}$, respectively. Besides confirming the flow rates measured at the weir, the ADV measurements indicate significant turbulence intensity throughout the water depth, with root mean square (RMS) fluctuations exceeding 10 % of the bulk velocity.

The hydrodynamic conditions at both ROIs are summarized in Table 1. The Reynolds number $\mathrm{Re} = DU_{bulk}/\nu$ and the Froude number $\mathrm{Fr} = U_{bulk}/\sqrt{gD}$ are based on the water depth $D$ and the bulk flow velocity $U_{bulk}$, both spatially averaged over the respective ROIs. $U_{bulk} = Q/A$ is calculated from the cross-sectional area $A$ inferred from the bathymetry, $g$ is the gravitational acceleration, and $\nu$ is the kinematic viscosity. Despite the Meander being

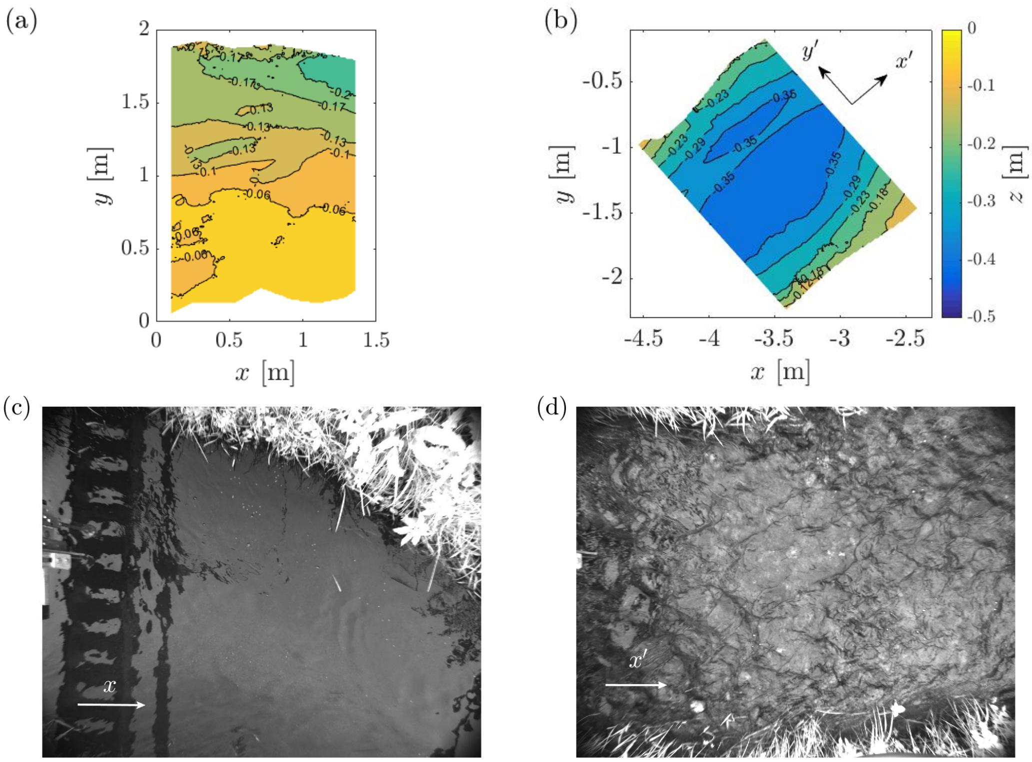


**Figure 2.** Bathymetry of the Meander (a) and Riffle (b) for $Q = 53.7\,\mathrm{L\,s^{-1}}$. Instantaneous photographs of the free-surface at the Meander (c) and Riffle (d) for the same flow rate, indicating the streamwise direction $x$ and $x'$, respectively.

shallower and associated to a larger Fr, the Riffle displays a wavier surface (Figure 2c-d) which is attributed to the turbulence induced by the rocky bed in this region (Brocchini & Peregrine, 2001). In both ROIs Fr $\ll 1$, and indeed the ultrasonic probe data indicates limited deformation of the free-surface: the RMS fluctuations of the water surface level are approximately 1 mm and 2 mm in the Meander and Riffle, respectively. Instantaneous images (acquired as described below) indicate wavelengths of 3 to 6 cm in the Meander and 4 to 8 cm in the Riffle. Thus, the estimated Stokes drift velocity is at least one order of magnitude smaller than the RMS velocity fluctuations measured by PTV, confirming that the waves do not significantly alter the transport of the floating particles in the considered flow.

### 2.2 Floating Particles

Three types of floating particles are used in the present experiments. White polypropylene bean-bag filler pellets, approximately spherical with a 5 mm diameter, are used to characterize the surface flow velocity. These are sufficiently large to be accurately detected by imaging and can be recaptured downstream of the ROIs. Systematic studies assessing the ability of floating particles to faithfully follow the surface turbulent fluctuations are scarce. In Nikora et al. (2007), 3 mm floating particles were deemed suitable as tracers for free-surface turbulence in a laboratory flume. The largest eddies in homogeneous turbulence have diameters several times larger than the Kolmogorov scale $\eta$ (Jiménez et al., 1993; Carter et al., 2016). Thus, neutrally buoyant particles up to $5\eta$ are typically considered faithful tracers (Fiabane et al., 2012), and even for particle sizes of $\sim 10\eta$ the response time

**Table 1.** Main hydrodynamic parameters of the Meander (a) and Riffle (b) for both volumetric flow rates $Q$: mean depth of the channel $D$, mean width of the channel $W$, mean cross-sectional area $A$, bulk fluid velocity $U_{bulk}$, Reynolds number Re, and Froude number Fr.

| (a) Meander | $D$ [m] | $W$ [m] | $A$ [m$^2$] | $U_{bulk}$ [m s$^{-1}$] | Re | Fr |
|---|---|---|---|---|---|---|
| $Q = 32.1$ L s$^{-1}$ | 0.08 | 1.72 | 0.143 | 0.225 | 18,480 | 0.25 |
| $Q = 53.7$ L s$^{-1}$ | 0.10 | 1.72 | 0.177 | 0.303 | 30,910 | 0.30 |

| (b) Riffle | $D$ [m] | $W$ [m] | $A$ [m$^2$] | $U_{bulk}$ [m s$^{-1}$] | Re | Fr |
|---|---|---|---|---|---|---|
| $Q = 32.1$ L s$^{-1}$ | 0.29 | 1.68 | 0.492 | 0.065 | 18,977 | 0.04 |
| $Q = 53.7$ L s$^{-1}$ | 0.31 | 1.68 | 0.525 | 0.102 | 31,750 | 0.06 |

**Table 2.** Summary of the main properties of the floating particles.

| Particle Type | Spheres (Tracers) | Discs | Rods |
|---|---|---|---|
| Material | Polypropylene | Wood | Wood |
| Density [g cm$^{-3}$] | 0.9 | 0.7 | 0.7 |
| Major Axis [mm] | 5.0 | 38.1 | 63.5 |
| Minor Axis [mm] | 5.0 | 38.1 | 1.8 |
| Thickness [mm] | — | 3.2 | — |

is about 1.5 times that of fluid tracers (Qureshi et al., 2007; Volk et al., 2011). As it will be shown, the estimated Kolmogorov length scale of the free-surface turbulence in the Meander is roughly 10 times smaller than the spherical pellets, which are 35 to 50 times smaller than the integral scale of the turbulence. Therefore, while these particles may not respond faithfully to the smallest-scale fluctuations, they capture most of the turbulent kinetic energy and will be regarded as tracers.

To explore the effect of shape and size on particle transport, larger discs and rods are utilized. The discs consist of wooden craft circles and the rods are wooden toothpicks, both spray-painted white to increase their visibility and to reduce their absorption of water. The different particle properties are summarized in Table 2. An estimate of the particle Stokes number St (the ratio of the particle response time to a relevant flow time scale) is not attempted. Directly measuring the response time to the fluid velocity fluctuations would require the accurate measurement of the particle acceleration autocorrelation, which is beyond the capability of the present imaging system. Theoretical expressions require assumptions on the drag exerted on the particles; this depends on their level of submergence (Beron-Vera et al., 2019), which cannot be accurately measured here.

### 2.3 Particle Imaging and Tracking

A 1-megapixel CMOS camera (Allied Vision Mako U-130B) with a 3 mm wide-angle lens is mounted on a cantilever arm attached to a traversing system composed of aluminum beams (Figure 1b). The camera is suspended 1.5 m above the water surface, imaging a 2.2 m $\times$ 1.7 m field of view (FOV). To minimize reflections on the water surface, a large tent is set up to enclose the camera and the FOV, blocking direct sunlight that would cause reflections and any wind that may affect the free-surface.

To recapture the floating particles, a nylon seine net is suspended from a PVC pipe frame across the channel 3 m downstream of the Meander. Particles are manually seeded onto the water surface by gently shaking a wide bin spanning the channel width upstream of the ROIs. The camera records at a frame rate of 30 to 50 Hz depending on the ROI and flow rate, keeping the inter-frame particle displacement to about 6 pixels. The measurements are performed over four runs for each case, to prevent the net from filling with particles and obstructing the water flow. This results in about 15,000 to 20,000 images, yielding approximately 16,000 particle trajectories for the tracers and 1,000 trajectories for the discs and rods, per each case. We verify that each run yields the same quantitative results for each case, thus statistical uncertainty due to finite sample size does not affect the conclusions.

The wide-angle camera lens introduces some image distortion. To correct it, a $0.9\,\mathrm{m} \times 1.2\,\mathrm{m}$ checkerboard pattern is imaged at the same distance as the water surface, and the appropriate de-warping transform is determined using MATLAB. Despite the tent blocking direct sunlight, some glare off the water surface from the diffused ambient light is still present. This time-dependent background noise is removed using the proper orthogonal decomposition (POD)-based method by Mendez et al. (2017), which isolates the modes mostly contributing to the intensity variance of the images. We subtract the first two modes, which successfully removes most of the glare while preserving the particle images.

Particles are identified as continuous groups of pixels exceeding an intensity threshold. Considering the probability distribution function (PDF) of the areas of these groups of pixels, a rejection criterion is set at $\pm 2$ standard deviations from the expected value (based on the pixel/mm ratio). Particle centroids are tracked using a custom-written nearest-neighbour PTV algorithm (Baker & Coletti, 2019, 2021), and their velocities and accelerations are obtained from the trajectories by convolution with the first and second derivative of a Gaussian kernel in the time domain, respectively. A temporal kernel of 16 frames is chosen as the shortest interval beyond which the acceleration variance decays exponentially. This approach has been used in several previous laboratory and field studies (Voth et al., 2002; Nemes et al., 2017; Li et al., 2022; Berk & Coletti, 2021; Baker & Coletti, 2021, 2022). We also characterize the rods' orientation and rotation rate along their trajectory. The orientation is defined by the unit vector $\hat{\mathbf{p}}$ aligned with the rod axis, obtained from an ellipse best-fit to the object image. The angular velocity $\omega$ is obtained convolving $\hat{\mathbf{p}}(t)$ with the first derivative of a Gaussian kernel, analogously to the particle velocity and using the same temporal kernel.

# 3 Results and discussion

## 3.1 Free-Surface Flow: Eulerian Fields

We first consider the Eulerian fields of the mean velocity $\tilde{U}$, and the RMS fluctuations $\tilde{\sigma}_u$. Here $U = \sqrt{U_x^2 + U_y^2}$ is the norm of the free-surface velocity vector $\mathbf{U}$ obtained by 2D imaging. The Eulerian data is obtained by binning the PTV trajectories in fixed interrogation windows of $5\,\mathrm{cm} \times 5\,\mathrm{cm}$ and indicated with a tilde. This allows for a temporal averaging of at least 25 instantaneous vectors in each window. The results for both measurement locations and flow rates are shown in Figure 3. The Meander displays a remarkably homogeneous surface flow. In particular, we define it in a $1.25 \times 1\,\mathrm{m}$ sub-region (highlighted in the figure) where $\tilde{U}$ and $\tilde{\sigma}_u$ remain within $\pm 2.5\,\%$ and $9.3\,\%$ of their respective spatial mean and the streamlines are relatively straight. This allows us to investigate unbiased single-point and two-point flow statistics, characterizing the spatio-temporal flow scales using the framework of homogeneous turbulence (presented in the next section). Lagrangian particle transport is investigated in the same sub-region.

The mean flow in the Riffle, on the other hand, resembles a jet-like flow with two shear layers associated to high velocity fluctuations and flanked by recirculation zones. Because of the large spatial inhomogeneity, the scales of the free-surface turbulence in the Riffle are not carried out using two-point statistics, as this would require spatial averaging and the evaluation of velocity fluctuations around a global mean. The Lagrangian particle transport in this ROI is quantified in a $1.1 \times 1\,\mathrm{m}$ sub-region. For both ROIs, the choice of the sub-

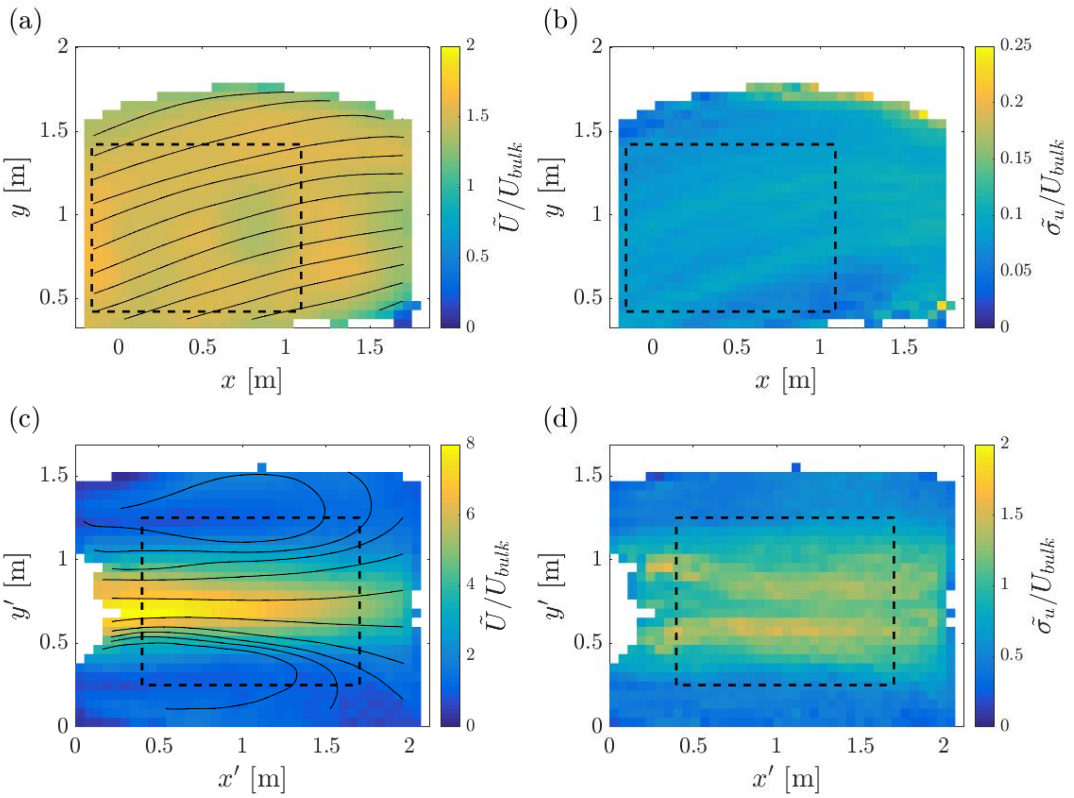


**Figure 3.** (a-c) Eulerian mean velocity and (b-d) RMS velocity fluctuation fields of the tracers for $Q = 32.1\,\mathrm{L\,s^{-1}}$, normalized by the bulk velocity; Meander (a-b) and Riffle (c-d). The black lines indicate streamlines and the dashed boxes indicate the sub-regions where Lagrangian quantities are evaluated.

region avoids that the statistics be strongly influenced by the proximity of the banks and reduces potential bias from short trajectories as the particles exit the FOV.

### 3.2 Free-surface Turbulence in the Meander

For a statistical analysis of the turbulence structure, we are particularly interested in the instantaneous velocity fluctuations. For this purpose, the velocity fluctuation $\mathbf{u}(t)$ is calculated by subtracting from the measured velocity $\mathbf{U}$ the global mean $\langle \mathbf{U} \rangle$, $\mathbf{U}(t) = \langle \mathbf{U} \rangle + \mathbf{u}(t)$. Here $t$ indicates time and angled brackets indicate ensemble-averaging over all realizations and all spatial locations within the homogeneous sub-region. Figure 4 displays the PDF of the streamwise ($u_x$) and spanwise ($u_y$) velocity fluctuations for $Q = 53.7\,\mathrm{L\,s^{-1}}$, as well as the PDF of the spanwise accelerations ($a_y$) for both flow rates; all quantities are normalized by their respective standard deviation. Both components of the velocity fluctuations appear normally distributed. On the other hand, the acceleration PDFs possess long exponential tails, indicating strong intermittency, i.e., relatively large probability of extreme events, especially for the higher Reynolds number. This behavior of Lagrangian accelerations has been well documented in 3D turbulence (Voth et al., 2002; Mordant et al., 2004; Toschi & Bodenschatz, 2009). While the kurtosis of the velocity fluctuations approximately equals the Gaussian value of 3, the acceleration kurtosis is 8.1 and 15.9 for $Q = 32.1\,\mathrm{L\,s^{-1}}$ and $Q = 53.7\,\mathrm{L\,s^{-1}}$, respectively. These levels of intermittency are typical of fully developed 3D turbulence (Voth et al., 2002; Ishihara et al., 2007).

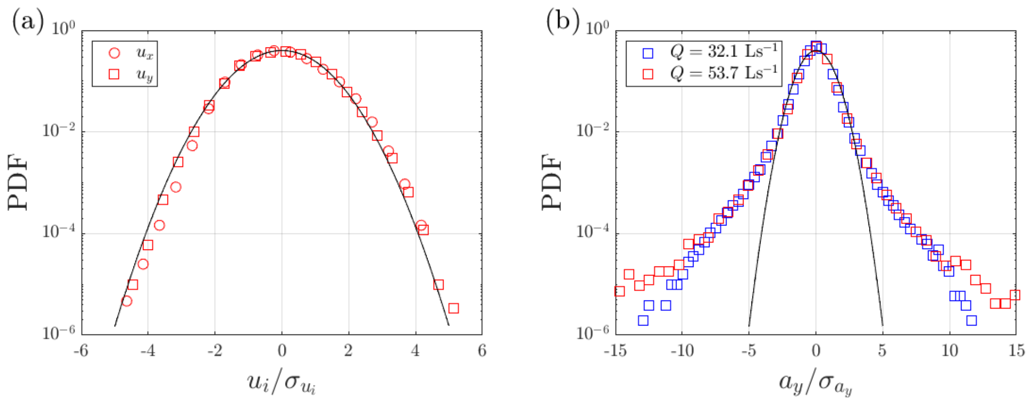


**Figure 4.** PDF of the streamwise and spanwise velocity fluctuations of the tracers in the Meander for $Q = 53.7\,\mathrm{L\,s^{-1}}$. (b) PDFs of the spanwise accelerations for both flow rates. The distributions are normalized by their respective standard deviations. The continuous line represents the normalized Gaussian distribution.

To characterize how the turbulent energy is distributed across the scales of the flow, we consider the Eulerian second-order structure function of the velocity fluctuations $S_2^E(\mathbf{r})$ (Kolmogorov, 1941; Pope, 2000). This is defined as the second moment of the velocity difference $\delta^E\mathbf{u}(\mathbf{r}) = \mathbf{u}(\mathbf{x}, t) - \mathbf{u}(\mathbf{x} + \mathbf{r}, t)$, where $\mathbf{u}(\mathbf{x}, t)$ and $\mathbf{u}(\mathbf{x} + \mathbf{r}, t)$ are the velocities of two particles separated by a distance $\mathbf{r}$ at a given time $t$. Leveraging spatial homogeneity, we ensemble-average over all particle pairs at a distance $r$:

$$S_2^E(\mathbf{r}) = \langle \delta^E\mathbf{u}(\mathbf{r})^2 \rangle \tag{1}$$

The ensemble-averaging requires binning the data over ranges of separation $r \pm \Delta r$, where we take $\Delta r = 1\,\mathrm{mm}$ as a trade-off between resolution in scale-space and statistical convergence. Here we focus on the longitudinal structure function, in which the velocity component parallel to the separation vector $\mathbf{r}$ is considered. Figure 5a shows that this exhibits an approximate $r^{2/3}$ scaling over separations from about 3 mm to 10 cm. This suggests the validity of the Kolmogorov (1941) ansatz in the inertial sub-range:

$$S_2^E(r) = C_2(\epsilon r)^{2/3} \tag{2}$$

where $\epsilon$ is the dissipation rate of the turbulent kinetic energy, and $C_2$ is a constant. While the applicability of Kolmogorov theory to free-surface turbulence is debated (Hunt & Graham, 1978; Magnaudet, 2003), experimental and numerical studies have documented a $k^{-5/3}$ scaling of the energy spectra at or near the free-surface (Chickadel et al., 2011; Flores et al., 2017), equivalent to the $r^{2/3}$ scaling of the second-order structure function. Flores et al. (2017) report that, even though the mechanism underlying the spectral slope at the surface may differ from the 3D turbulence dynamics in the bulk, the proportionality constants are roughly the same. Therefore, here we assume $C_2 = 2.1$ as in 3D turbulence (Pope, 2000; Saddoughi & Veeravalli, 1994) and use Equation 2 to estimate $\epsilon$ from the plateau of the compensated structure functions in Figure 5b. We then estimate the dissipative scales of the free-surface turbulence, i.e., the Kolmogorov length and time scales, respectively:

$$\eta = \left(\frac{\nu^3}{\epsilon}\right)^{1/4} \tag{3}$$

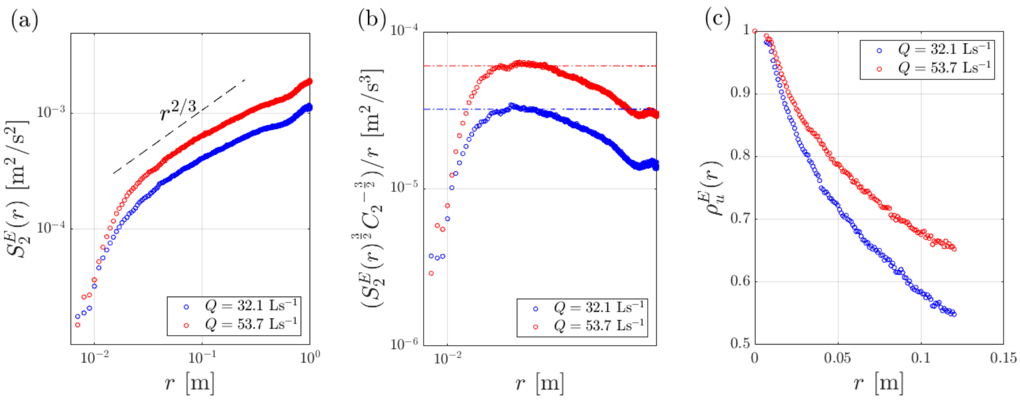


**Figure 5.** (a) Eulerian longitudinal second-order structure function, (b) compensated structure function and (c) Eulerian velocity autocorrelation function of the tracers for both flow rates. The dashed line in (a) corresponds to $r^{2/3}$ scaling. The dashed-dotted horizontal lines in (b) show the plateau of the compensated structure function which corresponds to the turbulent dissipation rate.

$$\tau_\eta = \left(\frac{\nu}{\epsilon}\right)^{1/2} \tag{4}$$

To determine the integral scales of the free-surface turbulence, we make use of the Eulerian velocity autocorrelation function, which in homogeneous isotropic turbulence can be calculated from the second-order structure function:

$$\rho_u^E(r) = \frac{\langle u(\mathbf{x},t)u(\mathbf{x}+\mathbf{r},t)\rangle}{\sigma_u^2} = 1 - \frac{S_2^E(r)}{2\sigma_u^2} \tag{5}$$

where $\sigma_u^2$ is the velocity variance. The velocity correlation exhibits an approximately exponential decay (Figure 5c), and the integral length scale $L$ is evaluated by least-square fitting to it a function $A\mathrm{e}^{-r/L}$, where $A$ is a constant of order unity. The estimates for the dissipative and integral scales, summarized in Table 3, support the notion that the $r^{2/3}$ scaling of the structure function applies over an inertial sub-range $\eta \ll r \ll L$. Additionally, an alternative estimate of the dissipation rate can be obtained from the classic scaling (Tennekes & Lumley, 1972):

$$\epsilon \approx C\frac{\sigma_u^3}{L} \tag{6}$$

Taking the proportionality constant $C = 0.5$ as typical for 3D turbulence in the high-Reynolds number limit (Burattini et al., 2005; Carter et al., 2016), we find dissipation estimates very close to those found from the second-order structure function (Table 3).

### 3.3 Effect of Particle Shape and Size in the Meander

In this section we compare the motion of the larger particles (discs and rods) against the tracers. We start by considering the Meander where the flow homogeneity allows for a comprehensive statistical description of the transport.

The Eulerian velocity fields of all particle types are found to be quantitatively similar. This is evident by comparing Figure 6a-b, where the mean velocity fields of the discs and

**Table 3.** Main physical quantities characterizing the free-surface turbulence for both flow rates in the Meander: RMS of the velocity fluctuations $\sigma_u$, intergral length scales $L$, dissipation rate of turbulent kinetic energy $\epsilon$, Kolmogorov length scale $\eta$, and Kolmogorov time scale $\tau_\eta$.

| Meander | $Q = 32.1\,\mathrm{L\,s^{-1}}$ | $Q = 53.7\,\mathrm{L\,s^{-1}}$ |
|---|---|---|
| $\sigma_u$ $[\mathrm{m\,s^{-1}}]$ | 0.022 | 0.032 |
| L [m] | 0.175 | 0.243 |
| $\epsilon$ from (2) $[\mathrm{m^2\,s^{-3}}]$ | $3.2 \cdot 10^{-5}$ | $6.1 \cdot 10^{-5}$ |
| $\epsilon$ from (6) $[\mathrm{m^2\,s^{-3}}]$ | $3.1 \cdot 10^{-5}$ | $6.6 \cdot 10^{-5}$ |
| $\eta$ [mm] | 0.4 | 0.4 |
| $\tau_\eta$ [s] | 0.18 | 0.13 |

rods are displayed for $Q = 32.1\,\mathrm{L\,s^{-1}}$, with the tracers in Figure 3a. For both considered flow rates, the RMS difference between the three particle types is less than 2 % of $\tilde{U}$ and less than 17 % of $\tilde{\sigma}_u$.

Figure 6 also displays PDFs of particle velocities and accelerations for selected components and flow rates. To highlight the difference between the different particle types, the Kolmogorov velocity scale $u_\eta = \eta/\tau_\eta$ and acceleration scale $a_\eta = u_\eta/\tau_\eta$ are used for normalization. The velocity fluctuations are similar between all particle types, closely approximating a Gaussian distribution (Figure 6c). On the other hand, the acceleration intermittency shown by the tracers is significantly reduced for the larger particles (Figure 6d). At $Q = 32.1\,\mathrm{L\,s^{-1}}$, the RMS acceleration of the discs and rods is 9 % and 21 % lower than that of the tracers, respectively; while at $Q = 53.7\,\mathrm{L\,s^{-1}}$ the reduction becomes 8 % and 20 %, respectively.

To characterize the spreading rate of the floating particles, we consider their Lagrangian motion characterized by single-particle and particle-pair dispersion. The former examines how far, on average, a single particle migrates from its origin over time. Leveraging the homogeneity of the flow in the Meander and following the classic framework of Taylor (1921), the single-particle diffusivity can be derived from the Lagrangian velocity autocorrelation:

$$\rho_u^L(\tau) = \left\langle \frac{\sum u(t)u(t+\tau)}{\sum u(t)^2} \right\rangle \tag{7}$$

Here the summation extends to all values of $\tau$ along each trajectory, i.e., the autocorrelation is first calculated along each trajectory and normalized by its velocity variance, before ensemble-averaging over all trajectories. This ensures that each trajectory has the same weight when contributing to the global autocorrelation coefficient (Guala et al., 2007). Additionally, we only consider trajectories whose duration is longer than the time delay $\tau$ (Mordant et al., 2004). Figure 7a-b display the Lagrangian velocity autocorrelation of each particle type for both considered flow rates, showing that the motion of the discs and rods is more time-correlated than that of the tracers. This is consistent with the trend reported by numerical simulations of inertial particles (Squires & Eaton, 1991; Jung et al., 2008) and laboratory observations of finite-size particles (Machicoane & Volk, 2016) in 3D turbulence.

The diffusivity $K$ is obtained by integrating the decaying Lagrangian velocity autocorrelation (Taylor, 1921):

$$K = \sigma_u^2 \int_0^\infty \rho_u^L(\tau) d\tau \tag{8}$$

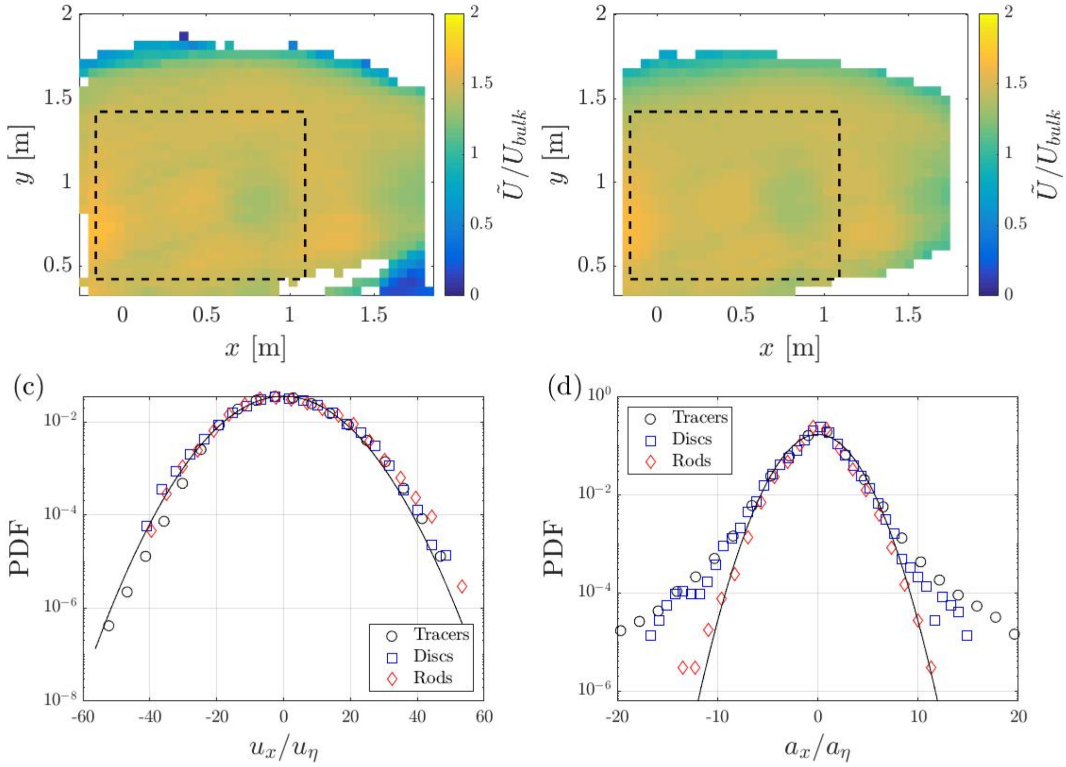


**Figure 6.** Eulerian mean velocity fields of the discs (a) and rods (b) for $Q = 32.1\,\mathrm{L\,s^{-1}}$. (c) PDFs of the streamwise velocity fluctuations of the different particle types in the Meander for $Q = 53.7\,\mathrm{L\,s^{-1}}$. (d) PDFs of the streamwise accelerations of the different particle types in the same location for $Q = 32.1\,\mathrm{L\,s^{-1}}$. The distributions are normalized by Kolmogorov scaling. The continuous line represents the normalized Gaussian distribution.

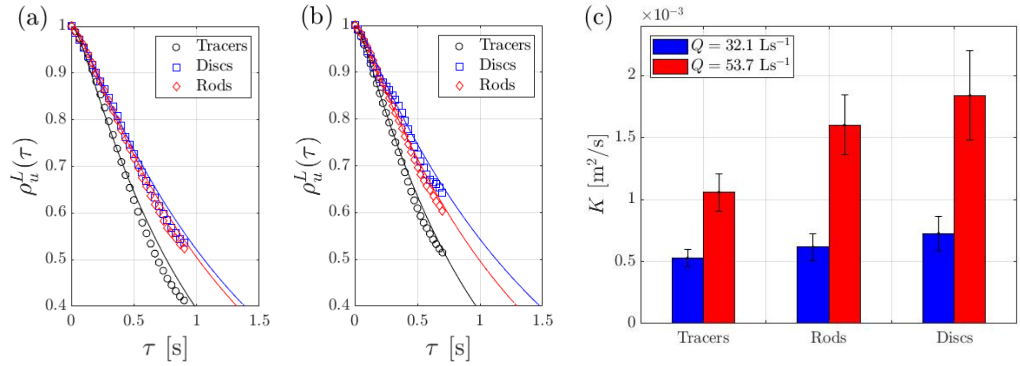


**Figure 7.** Lagrangian velocity autocorrelation function of each particle type for $Q = 32.1\,\mathrm{L\,s^{-1}}$ (a) and $Q = 53.7\,\mathrm{L\,s^{-1}}$ (b). The solid lines are the autocorrelation functions computed using Equation 9 which are integrated to obtain diffusion coefficients. (c) Diffusivity of the different particle types for both flow rates. The error bars represent the standard deviation of the diffusion coefficients from separate runs.

As the extreme of integration grows, the autocorrelation is expected to decay to negligibly small values and correspondently the diffusivity will asymptote to a value independent of time. Due to the finite length of the recorded trajectories, we extrapolate the autocorrelation using the stochastic model proposed by Sawford (1991):

$$\rho_u^L(\tau) = \frac{T_L \mathrm{e}^{-\tau/T_L} - T_2 \mathrm{e}^{-\tau/T_2}}{T_L - T_2} \tag{9}$$

Two time scales are required: the integral time scale of the turbulence $T_L$, and a characteristic time scale related to the dissipation $T_2$. The former is defined as the characteristic decay time of the Lagrangian velocity autocorrelation function and is estimated by least-square fitting $\rho_u^L(\tau)$ to an exponential function. The value of $T_2$ is estimated by fitting the experimental curve to Equation 9 and found to be approximately $0.3\tau_\eta$; this is the same order of magnitude as in 3D turbulence studies (Voth et al., 2002; Mordant et al., 2004). The diffusivity is then determined by the long-time asymptote of $K$. For the tracers we obtain normalized diffusivities $K/(u_\tau D) \approx 0.5$ for both flow rates, where we estimate the friction velocity $u_\tau$ from its relationship with the dissipation rate, $\epsilon = {u_\tau}^3/D$ (assumed to be mainly driven by bed friction (Raymond et al., 2012)). This falls well in the range $K/(u_\tau D) = 0.3$ to $0.9$ reported for meandering channels (Fischer et al., 1979; Rutherford, 1994). The diffusivity is plotted in Figure 7c for the different particle types and for both considered flow rates. One clearly sees an increase in $K$ with increasing flow rate, hence with Reynolds number. Most importantly, the larger particles exhibit larger diffusivity than the tracers, with the discs dispersing faster than the rods.

To verify this notion, we consider the mean square displacement (MSD) of the particles due to turbulent fluctuations:

$$\langle X(t)^2 \rangle = \langle \|\mathbf{x}(t) - \mathbf{x}(t_0) - \langle \mathbf{U} \rangle \Delta t\|^2 \rangle \tag{10}$$

where $\mathbf{x}(t)$ is the particle position at time $t$ and $\mathbf{x}(t_0)$ is the reference position at the temporal origin of the trajectory $t_0$. The advective displacement $\langle \mathbf{U} \rangle \Delta t$, due to the mean flow during the time interval $\Delta t = t - t_0$, is subtracted to isolate the contribution of the turbulent fluctuations. Leveraging spatial homogeneity, the advective flow is taken to be a uniform motion, which avoids the ambiguities associated to subtracting different advective displacements at different points along a same trajectory. The MSD of each particle type for both flow rates is plotted in Figure 8a-b and confirms that the discs spread faster than the rods, which spread faster than the tracers. We also note that MSD can alternatively be compute integrating the autocorrelation twice (Taylor, 1921; Pope, 2000):

$$\langle X(t)^2 \rangle = 2\sigma_u^2 \int_0^t \int_0^{t'} \rho_u^L(\tau) d\tau dt' \tag{11}$$

where $t'$ is a second integration variable. This yields analogous trends, not shown for brevity.

We then turn to pair-dispersion, quantified via the mean square separation (MSS):

$$\langle [D(t) - D(t_0)]^2 \rangle = \langle [\|\mathbf{x}_i(t) - \mathbf{x}_j(t)\| - D(t_0)]^2 \rangle \tag{12}$$

Here $\mathbf{x}_i(t)$ and $\mathbf{x}_j(t)$ are the positions of the $i$-th and $j$-th particles at time $t$, respectively. The initial separation $D(t_0) = \|\mathbf{x}_i(t_0) - \mathbf{x}_j(t_0)\|$ is subtracted to account for possible correlation between initial separation and relative velocity of the particle pair (Ouellette et al., 2006). The minimum distance between particle edges is typically 0.01 m, thus intermolecular effects as well as inter-particle capillary forces are negligible. Figure 8c-d shows the MSS of each particle type for $Q = 53.7\,\mathrm{L\,s^{-1}}$, in both linear and logarithmic axes. The

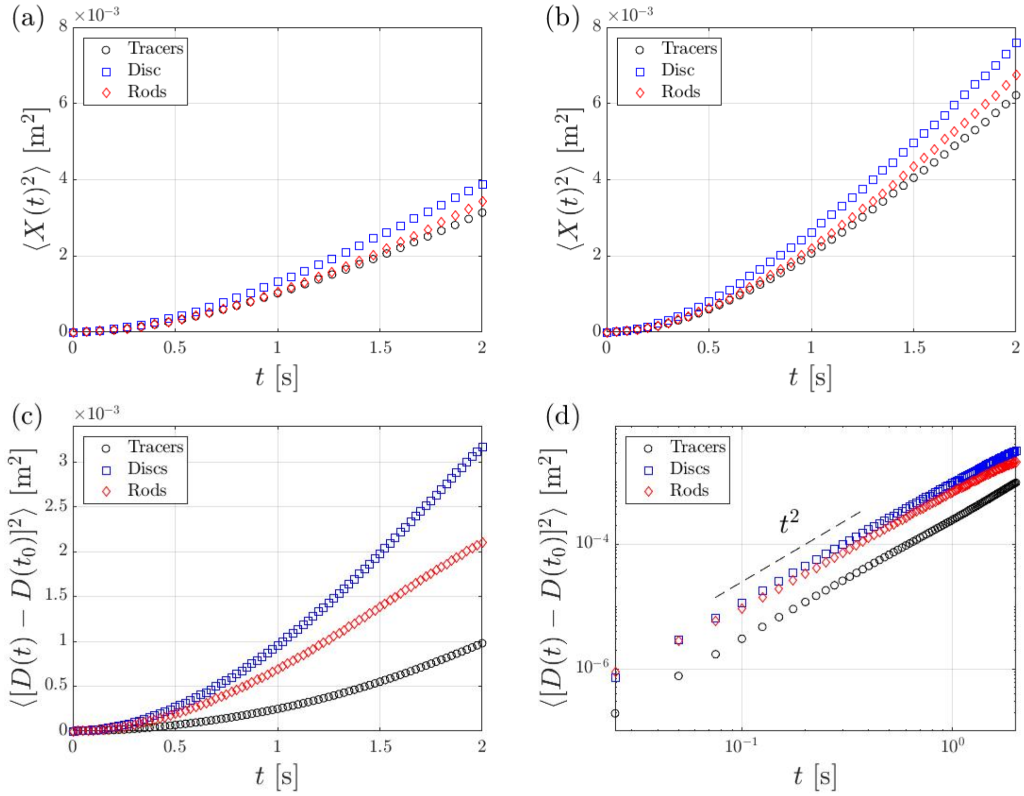


**Figure 8.** Mean square displacement due to turbulent velocity fluctuations of each particle type for $Q = 32.1\,\mathrm{L\,s^{-1}}$ (a) and $Q = 53.7\,\mathrm{L\,s^{-1}}$ (b). Mean square separation of each particle type for $Q = 53.7\,\mathrm{L\,s^{-1}}$, plotted in linear axes (c) and logarithmic axes (d). The dashed line in (d) corresponds to the $t^2$ (ballistic) scaling.

$t^2$ scaling predicted by Batchelor (1950) for particles in turbulence in the initial phase of separation is recovered, indicating ballistic separation in the considered regime and time scales. Consistently with the picture gained from the single-particle dispersion analysis, the discs separate from each other faster than the rods, and the latter separate faster than the tracers. We note that, for delays longer than the turnover time of eddies of size $D(t_0)$ (with $D(t_0)$ in the inertial sub-range), Richardson (1921) predicted super-diffusive dispersion with $D^2 \sim t^3$. However, such regime has been historically difficult to retrieve even in laboratory experiments (Bourgoin, 2015; Tan & Ni, 2022; Elsinga et al., 2022).

### 3.4 Effect of Particle Shape and Size in the Riffle

In this section we verify that the trends observed in the Meander also applies to the significantly different flow conditions found in the Riffle. Also here, the Eulerian fields of $\tilde{U}$ and $\tilde{\sigma_u}$ for the discs and rods (not shown) are close to those measured for the tracers and shown in Figure 5c-d, with RMS difference between the three particle types less than 12 % for $\tilde{U}$ and less than 16 % for $\tilde{\sigma_u}$. Nevertheless, as for the Meander, we shall see that the particle shape and size influences the Lagrangian dispersion.

Because the mean velocity in the Riffle is predominantly aligned with $x'$, we can isolate the turbulent dispersion by considering the lateral displacement, i.e., the MSD along the spanwise direction $y'$:

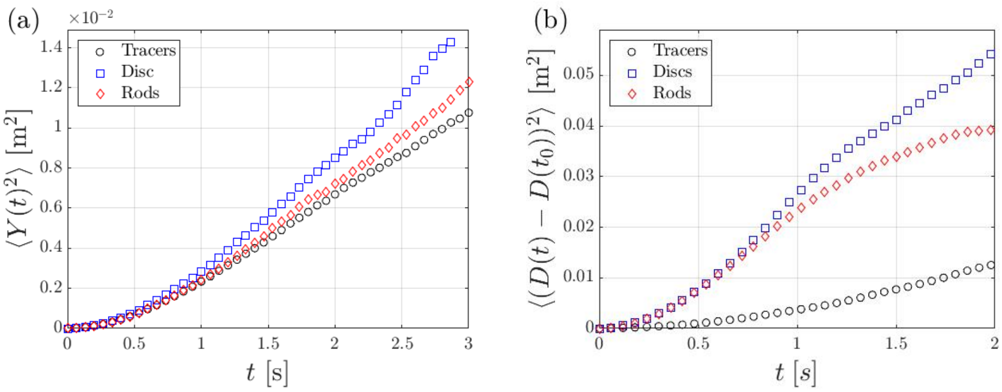


**Figure 9.** (a) Spanwise MSD of the different particles in the Riffle for $Q = 32.1\,\mathrm{L\,s^{-1}}$. (b) MSS of each particle type in the same location for $Q = 53.7\,\mathrm{L\,s^{-1}}$.

$$\langle Y(t)^2 \rangle = \langle [y'(t) - y'(t_0)]^2 \rangle \tag{13}$$

This is plotted in Figure 9a for $Q = 32.1\,\mathrm{L\,s^{-1}}$ ($Q = 53.7\,\mathrm{L\,s^{-1}}$ displaying analogous results). This indicates again that larger particles spread faster than the tracers, with the discs spreading faster than the rods. An estimate of the lateral diffusion coefficient can be derived from the relation:

$$K_{y'} = \frac{1}{2}\frac{d\langle Y(t)^2 \rangle}{dt} \tag{14}$$

A linear least-square fit to the data over the range $t > 1.5\,\mathrm{s}$ (where the MSD is approximately linear with time) yields $K_{y'}$ $=0.002\,\mathrm{m^2\,s^{-1}}$, $0.0025\,\mathrm{m^2\,s^{-1}}$ and $0.003\,\mathrm{m^2\,s^{-1}}$ for the tracers, rods, and discs, respectively. The same trend is retrieved for the particle-pair dispersion quantified by the MSS (Figure 9b), which is calculated as per Equation 12 for $Q = 53.7\,\mathrm{L\,s^{-1}}$. Both MSD and MSS indicate faster spreading rates in the Riffle compared to the Meander, which is expected due to the higher turbulence intensity $\sigma_u/U_{bulk}$ in the former.

### 3.5 Rotational dynamics

The translational and rotational motions of anisotropic particles in turbulence are strongly coupled to each other (Voth & Soldati, 2017). We therefore consider the rotational dynamics of the rods, as they can provide insight in the transport behaviour presented in the previous section. We present results for $Q = 53.7\,\mathrm{L\,s^{-1}}$, with $Q = 32.1\,\mathrm{L\,s^{-1}}$ showing analogous trends. We first consider the rod alignment defined by the orientation vector $\hat{\mathbf{p}}(t)$. Figure 10a shows the PDF of $|\hat{\mathbf{p}}(t) \cdot \hat{\mathbf{U}}(t)|$, where $\hat{\mathbf{U}}(t)$ is the unit vector parallel to the particle velocity. For both ROIs, the rods display a preference to align with the direction of motion. Considering the close similarity between the velocity fields of the tracers and those of the rods, this can be interpreted as a preferential alignment with the flow direction.

The curvature of the streamlines in the ROIs is small, but the rods orientation varies in time due to the flow fluctuations. We characterize the time scales associated to the rods' re-orientation by the Lagrangian autocorrelation of the particle orientation vector $\rho^L_{\hat{\mathbf{p}}}(\tau)$, calculated analogously to the velocity autocorrelation function in Equation 11 and shown in Figure 10b. In the Meander the particle orientation is remarkably stable, which is consistent with its moderate turbulence intensity: the fluid velocity, with which the rods tend to be aligned, remains mostly oriented in the streamwise direction. The orientation

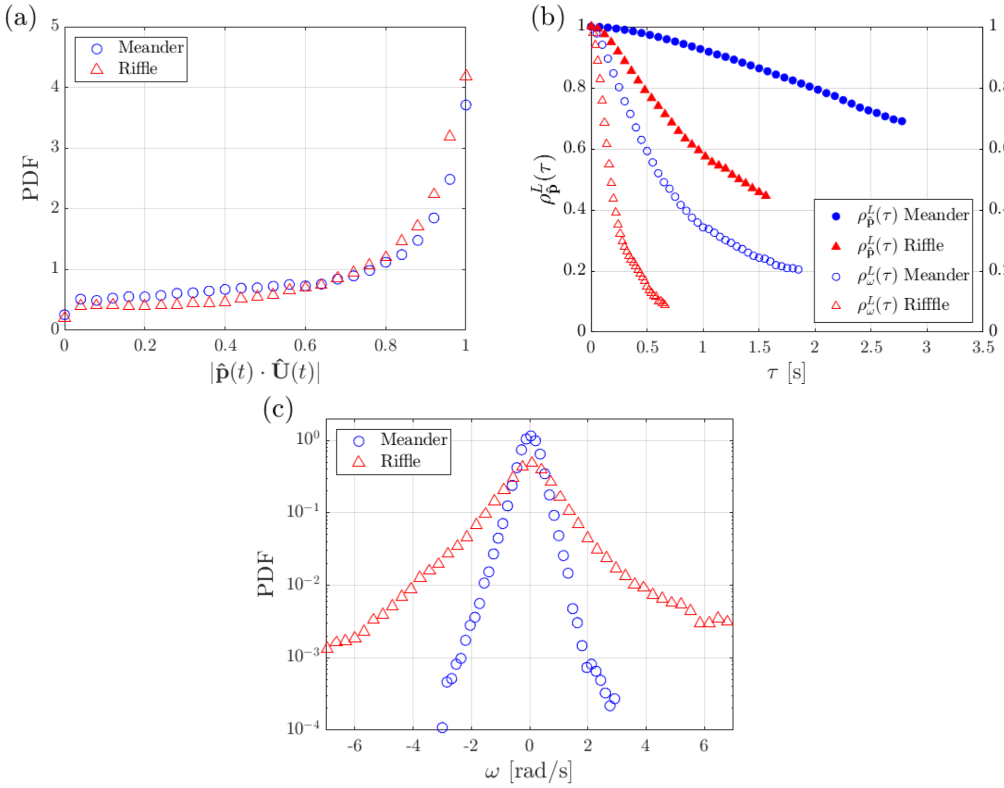


**Figure 10.** (a) PDF of the cosine of the orientation angle of the rods in both ROIs. (b) Lagrangian autocorrelation functions of the rods' orientation and angular velocity in both ROIs. (c) PDFs of the angular velocities in both ROIs.

autocorrelation in the Riffle shows a faster decay with a characteristic time of approximately 1.5 s. Given the jet-like flow structure, a candidate time scale dictating the rod reorientation is provided by the intense shear layers (Figure 5c-d). Indeed, visual observation confirms that the rods' rotation in those regions follows the direction of the mean flow shear. The associated time scale can be estimated from the jet half width, $d_{\frac{1}{2}} \approx 0.5\,\mathrm{m}$, and the velocity difference across it, $\Delta\tilde{U} \approx 0.4\,\mathrm{m\,s^{-1}}$: $d_{\frac{1}{2}}/\Delta\tilde{U} \approx 1.25\,\mathrm{s}$, which approximately agrees with the observed correlation time scale. The fact that the time scale of re-orientation be attributed to the mean shear of the surface flow is consistent with the observation that the rods' orientation is very stable in the Meander, where the flow is highly homogeneous and lateral shear is weak.

Figure 10b also shows the autocorrelation of the angular velocity $\rho^L_{\omega}(\tau)$, which as expected decays significantly faster than $\rho^L_{\mathbf{p}}(\tau)$. For the Meander, the correlation time scale of $\rho^L_{\omega}(\tau)$ is approximately 1 s, matching the integral time scale of the free-surface turbulence $T_L$. In the Riffle, the same quantity decays with a characteristic time scale around 0.25 s. While a single value of $T_L$ can hardly be defined in the Riffle due to spatial inhomogeneity, we note that $\tilde{\sigma_u}$ is roughly 4 times larger than in the Meander. This suggests that, in both ROIs, the correlation time scale of $\rho^L_{\omega}(\tau)$ is dictated by the energetic eddies that determine the integral scales of the turbulence. Since the rods' length is two orders of magnitude larger than $\eta$ and a fraction of $L$, this finding is in line with the view that rods' rotation is controlled by eddies of size comparable to or larger than their length (Parsa & Voth, 2014; Voth & Soldati, 2017).

The intermittent nature of the free-surface turbulence, displayed in the acceleration PDF in Figure 6d, is also reflected in the distribution of the angular velocity PDF shown in Figure 10c. The kurtosis of these distribution is 5.9 and 8.8 for the Meander and Riffle, respectively, indicating relatively large probability of extreme events with angular velocities of several $\mathrm{rad\,s^{-1}}$, especially with higher turbulence intensity of the free-surface. Such sudden changes in orientation are expected to alter the Lagrangian transport by the underlying flow.

## 4 Discussion

The PTV measurements of the small tracer particles, especially in the spatially homogeneous sub-region of the Meander, informs us on the nature of the free-surface flow in the considered riverine environment. We remark that, for fundamental reasons, free-surface turbulence is not expected to be equivalent to either 2D or to 3D turbulence: the surface exchanges energy and enstrophy with the flow underneath, hence neither quantity can be regarded as invariant and dimensional scaling arguments do not strictly apply (Cressman et al., 2004). However, the present measurements do indicate strong similarity with the phenomenology of 3D turbulence. In particular, the behaviour of the second-order structure function is consistent with Kolmogorov (1941) scaling in the inertial sub-range. While a similar scaling is also expected in the inverse-cascade range of 2D turbulence (Kraichnan, 1967), the latter framework is inconsistent with the observed intermittency of the acceleration (Boffetta & Ecke, 2012). The close agreement between the dissipation estimates from Equations 2 and 6 further supports the applicability of the 3D turbulence framework. The similarity between 3D and free-surface turbulence is possibly due to the surface carrying the prominent fingerprints of sub-surface vortices connected to it. These evolve by diffusion and stretching, as vortex tilting is annihilated at the surface (Shen et al., 1999; Zhang et al., 1999; Shen & Yue, 2001). In other words, unlike in 2D turbulence, the free-surface boundary condition affects but does not suppress vortex stretching, which is essential to the energy cascade in 3D turbulence (Davidson, 2015; Carbone & Bragg, 2020; Johnson, 2020). Our results are specific to a particular riverine flow configuration, therefore further studies are needed to assess the generality of the observations, especially for different water depths. Indeed, vortex stretching is hindered in shallow flows, which can trigger the emergence of features peculiar to 2D turbulence (Uijttewaal & Booij, 2000; Stocchino et al., 2011). Moreover, water depth influences the respective role of water-column turbulence and bed friction in setting the dissipation rate at the surface (Raymond et al., 2012; Ulseth et al., 2019).

Our main finding is that, in both investigated ROIs, larger floating particles disperse faster than smaller tracers. This result can be interpreted based on our understanding of the behaviour of inertial particles in turbulence. We remind that the term "inertial" indicates objects too heavy and/or too large to faithfully follow the fluid flow (Brandt & Coletti, 2022). Indeed, both discs and rods display weaker and less intermittent accelerations than the tracers. This behaviour is well known from the investigation of 3D turbulence laden with inertial particles and is attributed to two concurring mechanisms: preferential sampling of high-strain/low-vorticity regions, prevalent for small St; and inertial filtering of the small-scale/high-frequency fluctuations, prevalent for large St (Bec et al., 2006; Toschi & Bodenschatz, 2009). Although we do not evaluate St, the large size of the discs and rods compared to the Kolmogorov scales suggest that inertial filtering is the likely cause: the larger particles respond to a spatial average of the fluid velocity, making them less sensitive to the smaller and faster-decaying eddies. This is consistent with the increasingly time-correlated motion of the larger particles. The slower decay of the velocity autocorrelation is consistent with the simulations of Shin and Koch (2005) for rods in 3D turbulence, who found the correlation time scale $T_L$ to increase with the rods' length. However, in such study the RMS velocity fluctuations of the rods $\sigma_u$ was found to decrease with their length, and the diffusivity $K = {\sigma_u}^2 T_L$ ultimately decreased. Vice versa, in the present case, the RMS velocity fluctuations of the particles are not significantly affected by their size and shape, and thus the diffusivity follows the same trend as $T_L$. This different outcome with respect to Shin and Koch (2005) could be rooted in qualitative differences between free-surface and 3D turbulence. Another possible explanation is the range of scales at play: their simulations reached relatively low Reynolds numbers, with a range of scales $L/\eta < 30$, and were focused on rods of length comparable to or larger than the integral scales. On the other hand, in the present study $L/\eta$ exceeds 600, and the particle size is at most one third of the integral scale. Therefore, the floating discs and rods filter out only a fraction of the fluctuating energy contained in the large eddies, and therefore their velocity variance remains close to that of tracers.

Despite the rods' length being almost twice the discs' diameter, the latter disperse faster than the former. This may be due to the discs possessing a larger wetted area, thus more effective filtering of the small-scale fluctuations. However, the object shape is also likely to have a profound influence on the Lagrangian transport. The characteristic time scale of the angular velocity and its intermittent nature indicate that the instantaneous orientation of the rods is affected by a range of turbulent scales. These may contribute to decorrelating their translational motion, which for anisotropic particles is strongly coupled with the rotational motion (Voth & Soldati, 2017). Moreover, the rods' tendency to align with the flow direction suggests that the large scales of the turbulence (at least those larger than the rods' length) are not isotropic but likely populated by streamwise-oriented structures. Indeed, already early studies of open channel flows highlighted the connection between near-wall bursts in the bottom-wall boundary layer and the coherent motions that transfer mass to and from the free-surface (Nakagawa & Nezu, 1981; Rashidi & Banerjee, 1988). The complex bed topography of a natural channel is likely to enhance this connection by generating energetic eddies that can travel up to the surface, as indicated by the fact that bed roughness in shallow streams strongly correlates with gas transfer velocity (Ulseth et al., 2019).

Besides shape and size, other properties of floating particles may be influential towards their free-surface transport; in particular, bulk density and surface characteristics. Particles of higher density and mass may be more effective in filtering small-scale turbulent fluctuations, which could further enhance their diffusivity. However, depending on the size, this effect could be counteracted by a lack of responsiveness to some of the energetic scales responsible for the dispersion. Moreover, density and surface characteristics, in particular hydrophobicity, will affect the balance between surface tension and gravity, determining the submerged fraction of the floating object (Koh et al., 2009; Ji et al., 2018). In turn, submergence will determine the amount of windage, i.e., the drag exerted by the airflow on objects partly protruding out of the water (Zambianchi et al., 2014; Beron-Vera et al., 2019). Finally, while we have limited our study to sparse objects that do not significantly interact with each other, compressibility of the free-surface flow is known to produce intense clustering that can bring the floaters in close contact (Cressman et al., 2004; Lovecchio et al., 2013). Again, the material properties of the particles are then expected to affect the short-range interactions and possibly lead to aggregation (Vella & Mahadevan, 2005). The impact of such particle properties, which is outside the scope of the present work, clearly warrants further systematic investigations using different particle materials.

The observed influence of the particles' properties on dispersion, once confirmed for a wider range of particle types and flow conditions, may have profound implications for the transport of floating particles; in particular, the transport of meso- and macroplastics in small streams and turbulent waters in general. The diffusivity, which we find to roughly double from mm-sized to cm-sized objects, is a crucial quantity to incorporate the effect of unresolved spatio-temporal scales in Lagrangian transport models for rivers, lakes, and the oceans (Liu et al., 2011; Park et al., 2017; van Sebille et al., 2018; Daily & Hoffman, 2020; McDonald & Nelson, 2021). Our results indicate that such parameter varies significantly not only with the flow conditions, but also with the particle properties. Parameterizations that include also the latter appear necessary to obtain accurate predictions from such models.

## 5 Conclusion

Motivated by the need of understanding the transport of plastic litter in river flows, we have used time-resolved PTV to characterize the motion of particles of different shape and size floating on the surface of a field-scale meandering stream. We have considered two locations with different turbulence levels, in which the role of surface waves on the transport is deemed negligible. We have measured the position, velocity, and acceleration along the trajectories of thousands of millimetre-sized spherical pellets and centimetre-sized discs and rods, as well as the orientation and rotation of the latter, and evaluated the spatio-temporal scales associated with such quantities. At the Meander, the homogeneity of the flow properties allows us to identify both dissipative and integral scales of the free-surface turbulence, providing essential terms of comparison for the size of the particles and the scales of their motion. The spheres are small enough to capture most if not all scales of the free-surface motion and are regarded as flow tracers; while the length of the rods and the diameter of the discs are $\mathcal{O}(100)$ times larger than the dissipative scales and several time smaller than the integral scales of the turbulence. The analysis of the particles' motion leads to the following observations:

I. All considered particles displays almost indistinguishable mean velocities and RMS velocity fluctuations. These are determined by the largest scales of the surface flow, to which the particles respond faithfully.

II. While the velocity fluctuations follow normal distributions unaffected by the particle shape and size, the accelerations show a sizeable degree of intermittency which decreases for larger particles. This is attributed to the finite-size of the particles, filtering out the smallest scales of the turbulence associated to the most intense gradients.

III. Concequently, the larger particles spread more rapidly on the turbulent free-surface, with diffusivity coefficients roughly doubling for centimetre-sized particles as compared to millimetre-sized tracers. This is due to the motion of the larger particles being more time-correlated, which in turn is rooted in their impaired response to the small-scale turbulent fluctuations.

IV. The rods tend to align with the flow direction, but their instantaneous orientation is influenced by a range of scales: they re-orient following the mean shear, rotate according to the turnover time of the energetic eddies, and exhibit intermittency in their angular velocities. This leads to less time-correlated motions and slower dispersion than the discs, despite the rods' length being larger than the discs' diameter.

Overall, the behaviour of the free-surface turbulence and the motion of particles floating on it appears consistent with the phenomenology of inertial finite-sized particles in 3D turbulence. This similarity, to be confirmed in a wider range of flow conditions and particle types, may allow leveraging of established results and recent advances in the field of particle-laden turbulence (Balachandar & Eaton, 2010; Brandt & Coletti, 2022), furthering the predictive understanding of the transport of floating plastics in natural waters.

Future studies shall expand the present work in several directions. Our experiments have been carried out in a relatively small stream; studies in larger and deeper rivers, in which the dissipation mechanisms in the water column are inherently different (Moog & Jirka, 1999), are needed to expand and generalize the results. In such cases, particle imaging may require the use of uncrewed aerial vehicles, which have been successfully utilized to characterize natural flows (Blois et al., 2016; Liu et al., 2021). Given the variety of debris types found in water streams, the range of particle properties should be expanded beyond shape, size, and density: deformability and brittleness have recently been investigated in laboratory studies and are especially relevant to plastic pollution (Brouzet et al., 2014, 2021). Finally, high-Froude streams and/or under the action of wind, breaking and non-breaking waves may play a major role in the transport of floating particles. The recent laboratory experiments of Lenain et al. (2019), confirming computational results by Deike et al. (2017), found that breaking waves induce much stronger transport of cm-sized spherical particles compared to Stokes drift. Studies investigating the effect of particle properties in similar situations are warranted.

## Data Availability Statement

The pre-processed background-subtracted images for the different regions of interest, flow rates and particles are available at `https://doi.org/10.3929/ethz-b-000572787`.

## Acknowledgments

This work was supported by the Environmental and Natural Resources Trust Fund (ESF # 3015-11107-00064675) whose purpose is to provide a long-term, consistent, and stable source of funding for activities that protect, conserve, preserve and enhance Minnesota's air, water, land, fish, wildlife and other natural resources for the benefit of current citizens and future generations. The authors would like to thank Eleanor Arpin and SAFL technical staff for their assistance as well as the Legislative-Citizen Commission on Minnesota Resources (LCCMR) for their funding recommendation to the Minnesota Legislature.

## References

Adrian, R. J., & Westerweel, J. (2011). *Particle image velocimetry* (No. 30). Cambridge University Press.

Baker, L. J., & Coletti, F. (2019). Experimental study of negatively buoyant finite-size particles in a turbulent boundary layer up to dense regimes. *Journal of Fluid Mechanics*, *866*, 598–629.

Baker, L. J., & Coletti, F. (2021). Particle–fluid–wall interaction of inertial spherical particles in a turbulent boundary layer. *Journal of Fluid Mechanics*, *908*.

Baker, L. J., & Coletti, F. (2022). Experimental investigation of inertial fibres and disks in a turbulent boundary layer. *Journal of Fluid Mechanics*, *943*.

Balachandar, S., & Eaton, J. K. (2010). Turbulent dispersed multiphase flow. *Annual Review of Fluid Mechanics*, *42*, 111–133.

Batchelor, G. (1950). The application of the similarity theory of turbulence to atmospheric diffusion. *Quarterly Journal of the Royal Meteorological Society*, *76*(328), 133–146.

Bec, J., Biferale, L., Boffetta, G., Celani, A., Cencini, M., Lanotte, A., ... Toschi, F. (2006). Acceleration statistics of heavy particles in turbulence. *Journal of Fluid Mechanics*, *550*, 349–358.

Berk, T., & Coletti, F. (2021). Dynamics of small heavy particles in homogeneous turbulence: a lagrangian experimental study. *Journal of Fluid Mechanics*, *917*.

Beron-Vera, F. J., Olascoaga, M. J., & Miron, P. (2019). Building a maxey–riley framework for surface ocean inertial particle dynamics. *Physics of Fluids*, *31*(9), 096602.

Blois, G., Best, J., Christensen, K., Cichella, V., Donahue, A., Hovakimyan, N., ... Pakrasi, I. (2016). Assessing the use of uav to quantify flow processes in rivers. In *River flow.*

Boffetta, G., & Ecke, R. E. (2012). Two-dimensional turbulence. *Annual Review of Fluid Mechanics*, *44*(1), 427–451.

Bourgoin, M. (2015). Turbulent pair dispersion as a ballistic cascade phenomenology. *Journal of Fluid Mechanics*, *772*, 678–704.

Brandt, L., & Coletti, F. (2022). Particle-laden turbulence: progress and perspectives. *Annual Review of Fluid Mechanics*, *54*, 159–189.

Brocchini, M., & Peregrine, D. (2001). The dynamics of strong turbulence at free surfaces. part 1. description. *Journal of Fluid Mechanics*, *449*, 225–254.

Brouzet, C., Guiné, R., Dalbe, M.-J., Favier, B., Vandenberghe, N., Villermaux, E., & Verhille, G. (2021). Laboratory model for plastic fragmentation in the turbulent ocean. *Physical Review Fluids*, *6*(2), 024601.

Brouzet, C., Verhille, G., & Le Gal, P. (2014). Flexible fiber in a turbulent flow: A macroscopic polymer. *Physical Review Letters*, *112*(7), 074501.

Burattini, P., Lavoie, P., & Antonia, R. A. (2005). On the normalized turbulent energy dissipation rate. *Physics of Fluids*, *17*(9), 098103.

Carbone, M., & Bragg, A. D. (2020). Is vortex stretching the main cause of the turbulent energy cascade? *Journal of Fluid Mechanics*, *883*.

Carter, D., Petersen, A., Amili, O., & Coletti, F. (2016). Generating and controlling homogeneous air turbulence using random jet arrays. *Experiments in Fluids*, *57*(12), 1–15.

Chickadel, C. C., Talke, S. A., Horner-Devine, A. R., & Jessup, A. T. (2011). Infrared-based measurements of velocity, turbulent kinetic energy, and dissipation at the water surface in a tidal river. *IEEE Geoscience and Remote Sensing Letters*, *8*(5), 849–853.

Cressman, J. R., Davoudi, J., Goldburg, W. I., & Schumacher, J. (2004). Eulerian and lagrangian studies in surface flow turbulence. *New Journal of Physics*, *6*(1), 53.

Daily, J., & Hoffman, M. J. (2020). Modeling the three-dimensional transport and distribution of multiple microplastic polymer types in lake erie. *Marine Pollution Bulletin*, *154*, 111024.

Davidson, P. A. (2015). *Turbulence: an introduction for scientists and engineers.* Oxford university press.

Deike, L., Pizzo, N., & Melville, W. K. (2017). Lagrangian transport by breaking surface waves. *Journal of Fluid Mechanics*, *829*, 364–391.

DiBenedetto, M. H. (2020). Non-breaking wave effects on buoyant particle distributions. *Frontiers in Marine Science*, *7*, 148.

DiBenedetto, M. H., Koseff, J. R., & Ouellette, N. T. (2019). Orientation dynamics of nonspherical particles under surface gravity waves. *Physical Review Fluids*, *4*(3), 034301.

DiBenedetto, M. H., Ouellette, N. T., & Koseff, J. R. (2018). Transport of anisotropic particles under waves. *Journal of Fluid Mechanics*, *837*, 320–340.

Elsinga, G., Ishihara, T., & Hunt, J. (2022). Non-local dispersion and the reassessment of richardson's t3-scaling law. *Journal of Fluid Mechanics*, *932*.

Eriksen, M., Mason, S., Wilson, S., Box, C., Zellers, A., Edwards, W., ... Amato, S. (2013). Microplastic pollution in the surface waters of the laurentian great lakes. *Marine Pollution Bulletin*, *77*(1-2), 177–182.

Fiabane, L., Zimmermann, R., Volk, R., Pinton, J.-F., & Bourgoin, M. (2012). Clustering of finite-size particles in turbulence. *Physical Review E*, *86*(3), 035301.

Fischer, H. B., List, J. E., Koh, C. R., Imberger, J., & Brooks, N. H. (1979). *Mixing in inland and coastal waters.* Academic press.

Flores, O., Riley, J. J., & Horner-Devine, A. R. (2017). On the dynamics of turbulence near a free surface. *Journal of Fluid Mechanics*, *821*, 248–265.

Geyer, R., Jambeck, J. R., & Law, K. L. (2017). Production, use, and fate of all plastics ever made. *Science Advances*, *3*(7), e1700782.

Gomit, G., Chatellier, L., & David, L. (2022). Free-surface flow measurements by non-intrusive methods: a survey. *Experiments in Fluids*, *63*(6), 1–25.

Guala, M., Liberzon, A., Tsinober, A., & Kinzelbach, W. (2007). An experimental investigation on lagrangian correlations of small-scale turbulence at low reynolds number. *Journal of Fluid Mechanics*, *574*, 405–427.

Herlina, H., & Wissink, J. (2014). Direct numerical simulation of turbulent scalar transport across a flat surface. *Journal of Fluid Mechanics*, *744*, 217–249.

Hunt, J., & Graham, J. (1978). Free-stream turbulence near plane boundaries. *Journal of Fluid Mechanics*, *84*(2), 209–235.

Ishihara, T., Kaneda, Y., Yokokawa, M., Itakura, K., & Uno, A. (2007). Small-scale statistics in high-resolution direct numerical simulation of turbulence: Reynolds number dependence of one-point velocity gradient statistics. *Journal of Fluid Mechanics*, *592*, 335–366.

Jambeck, J. R., Geyer, R., Wilcox, C., Siegler, T. R., Perryman, M., Andrady, A., ... Law, K. L. (2015). Plastic waste inputs from land into the ocean. *Science*, *347*(6223), 768–771.

Ji, B., Song, Q., & Yao, Q. (2018). Limit for small spheres to float by dynamic analysis. *Langmuir*, *34*(34), 10163–10168.

Jiménez, J., Wray, A. A., Saffman, P. G., & Rogallo, R. S. (1993). The structure of intense vorticity in isotropic turbulence. *Journal of Fluid Mechanics*, *255*, 65–90.

Jin, T., & Liao, Q. (2019). Application of large scale piv in river surface turbulence measurements and water depth estimation. *Flow Measurement and Instrumentation*, *67*, 142–152.

Johnson, P. L. (2020). Energy transfer from large to small scales in turbulence by multiscale nonlinear strain and vorticity interactions. *Physical Review Letters*, *124*(10), 104501.

Jung, J., Yeo, K., & Lee, C. (2008). Behavior of heavy particles in isotropic turbulence. *Physical Review E*, *77*(1), 016307.

Koh, P., Hao, F., Smith, L., Chau, T., & Bruckard, W. (2009). The effect of particle shape and hydrophobicity in flotation. *International Journal of Mineral Processing*, *93*(2), 128–134.

Kolmogorov, A. N. (1941). The local structure of turbulence in incompressible viscous fluid for very large reynolds numbers. *Proceedings of the URSS Academy of Sciences*, *30*, 301–305.

Kraichnan, R. H. (1967). Inertial ranges in two-dimensional turbulence. *The Physics of Fluids*, *10*(7), 1417–1423.

Kumar, S., Gupta, R., & Banerjee, S. (1998). An experimental investigation of the characteristics of free-surface turbulence in channel flow. *Physics of Fluids*, *10*(2), 437–456.

Lebreton, L., Slat, B., Ferrari, F., Sainte-Rose, B., Aitken, J., Marthouse, R., ... Reisser, J. (2018). Evidence that the great pacific garbage patch is rapidly accumulating plastic. *Scientific Reports*, *8*(1), 1–15.

Lenain, L., Pizzo, N., & Melville, W. K. (2019). Laboratory studies of lagrangian transport by breaking surface waves. *Journal of Fluid Mechanics*, *876*.

Li, Y., Amili, O., & Coletti, F. (2022). Experimental study of concentrated particle transport in successively bifurcating vessels. *Physical Review Fluids*, *7*(8), 083101.

Liu, W.-C., Chen, W.-B., & Hsu, M.-H. (2011). Using a three-dimensional particle-tracking model to estimate the residence time and age of water in a tidal estuary. *Computers & Geosciences*, *37*(8), 1148–1161.

Liu, W.-C., Lu, C.-H., & Huang, W.-C. (2021). Large-scale particle image velocimetry to measure streamflow from videos recorded from unmanned aerial vehicle and fixed imaging system. *Remote Sensing*, *13*(14), 2661.

Lovecchio, S., Marchioli, C., & Soldati, A. (2013). Time persistence of floating-particle clusters in free-surface turbulence. *Physical Review E*, *88*(3), 033003.

Machicoane, N., & Volk, R. (2016). Lagrangian velocity and acceleration correlations of large inertial particles in a closed turbulent flow. *Physics of Fluids*, *28*(3), 035113.

Magnaudet, J. (2003). High-reynolds-number turbulence in a shear-free boundary layer: revisiting the hunt–graham theory. *Journal of Fluid Mechanics*, *484*, 167–196.

McDonald, R. R., & Nelson, J. M. (2021). A lagrangian particle-tracking approach to modelling larval drift in rivers. *Journal of Ecohydraulics*, *6*(1), 17–35.

McKenna, S., & McGillis, W. (2004). The role of free-surface turbulence and surfactants in air–water gas transfer. *International Journal of Heat and Mass Transfer*, *47*(3), 539–553.

Meijer, L. J., van Emmerik, T., van der Ent, R., Schmidt, C., & Lebreton, L. (2021). More than 1000 rivers account for 80% of global riverine plastic emissions into the ocean. *Science Advances*, *7*(18), 5803.

Mendez, M., Raiola, M., Masullo, A., Discetti, S., Ianiro, A., Theunissen, R., & Buchlin, J.-M. (2017). Pod-based background removal for particle image velocimetry. *Experimental Thermal and Fluid Science*, *80*, 181–192.

Miozzi, M., Lalli, F., & Romano, G. (2010). Experimental investigation of a free-surface turbulent jet with coanda effect. *Experiments in Fluids*, *49*(1), 341–353.

Miozzi, M., & Romano, G. P. (2020). Propagation of perturbations and meandering in a free surface shallow water jet. *Experiments in Fluids*, *61*(9), 1–18.

Moog, D. B., & Jirka, G. H. (1999). Air-water gas transfer in uniform channel flow. *Journal of Hydraulic Engineering*, *125*(1), 3–10.

Mordant, N., Lévêque, E., & Pinton, J.-F. (2004). Experimental and numerical study of the lagrangian dynamics of high reynolds turbulence. *New Journal of Physics*, *6*(1), 116.

Nakagawa, H., & Nezu, I. (1981). Structure of space-time correlations of bursting phenomena in an open-channel flow. *Journal of Fluid Mechanics*, *104*, 1–43.

Nemes, A., Dasari, T., Hong, J., Guala, M., & Coletti, F. (2017). Snowflakes in the atmospheric surface layer: observation of particle–turbulence dynamics. *Journal of Fluid Mechanics*, *814*, 592–613.

Nikora, V., Nokes, R., Veale, W., Davidson, M., & Jirka, G. (2007). Large-scale turbulent structure of uniform shallow free-surface flows. *Environmental Fluid Mechanics*, *7*(2), 159–172.

Ouellette, N. T., Xu, H., Bourgoin, M., & Bodenschatz, E. (2006). An experimental study of turbulent relative dispersion models. *New Journal of Physics*, *8*(6), 109.

Pan, Y., & Banerjee, S. (1995). A numerical study of free-surface turbulence in channel flow. *Physics of Fluids*, *7*(7), 1649–1664.

Park, I., Seo, I. W., Kim, Y. D., & Han, E. J. (2017). Turbulent mixing of floating pollutants at the surface of the river. *Journal of Hydraulic Engineering*, *143*(8), 04017019.

Parsa, S., & Voth, G. A. (2014). Inertial range scaling in rotations of long rods in turbulence. *Physical Review Letters*, *112*(2), 024501.

Parsheh, M., Sotiropoulos, F., & Porté-Agel, F. (2010). Estimation of power spectra of acoustic-doppler velocimetry data contaminated with intermittent spikes. *Journal of Hydraulic Engineering*, *136*(6), 368–378.

Pope, S. B. (2000). *Turbulent flows.* Cambridge university press.

Qureshi, N. M., Bourgoin, M., Baudet, C., Cartellier, A., & Gagne, Y. (2007). Turbulent transport of material particles: an experimental study of finite size effects. *Physical Review Letters*, *99*(18), 184502.

Raffel, M., Willert, C. E., Scarano, F., Kähler, C. J., Wereley, S. T., & Kompenhans, J. (2018). Image evaluation methods for piv. In *Particle image velocimetry* (pp. 145–202). Springer.

Rashidi, M., & Banerjee, S. (1988). Turbulence structure in free-surface channel flows. *The Physics of Fluids*, *31*(9), 2491–2503.

Raymond, P. A., Zappa, C. J., Butman, D., Bott, T. L., Potter, J., Mulholland, P., . . . Newbold, D. (2012). Scaling the gas transfer velocity and hydraulic geometry in streams and small rivers. *Limnology and Oceanography: Fluids and Environments*, *2*(1), 41–53.

Richardson, L. F. (1921). I. some measurements of atmospheric turbulence. *Philosophical Transactions of the Royal Society of London. Series A, Containing Papers of a Mathematical or Physical Character*, *221*(582-593), 1–28.

Rutherford, J. C. (1994). *River mixing.* Wiley.

Saddoughi, S. G., & Veeravalli, S. V. (1994). Local isotropy in turbulent boundary layers at high reynolds number. *Journal of Fluid Mechanics*, *268*, 333–372.

Sawford, B. (1991). Reynolds number effects in lagrangian stochastic models of turbulent dispersion. *Physics of Fluids A: Fluid Dynamics*, *3*(6), 1577–1586.

Shen, L., & Yue, D. K. (2001). Large-eddy simulation of free-surface turbulence. *Journal of Fluid Mechanics*, *440*, 75–116.

Shen, L., Zhang, X., Yue, D. K., & Triantafyllou, G. S. (1999). The surface layer for free-surface turbulent flows. *Journal of Fluid Mechanics*, *386*, 167–212.

Shin, M., & Koch, D. L. (2005). Rotational and translational dispersion of fibres in isotropic turbulent flows. *Journal of Fluid Mechanics*, *540*, 143–173.

Squires, K. D., & Eaton, J. K. (1991). Measurements of particle dispersion obtained from direct numerical simulations of isotropic turbulence. *Journal of Fluid Mechanics*, *226*, 1–35.

Stocchino, A., Besio, G., Angiolani, S., & Brocchini, M. (2011). Lagrangian mixing in straight compound channels. *Journal of Fluid Mechanics*, *675*, 168–198.

Tan, S., & Ni, R. (2022). Universality and intermittency of pair dispersion in turbulence. *Physical Review Letters*, *128*(11), 114502.

Tauro, F., Petroselli, A., Porfiri, M., Giandomenico, L., Bernardi, G., Mele, F., … Grimaldi, S. (2016). A novel permanent gauge-cam station for surface-flow observations on the tiber river. *Geoscientific Instrumentation, Methods and Data Systems*, *5*(1), 241–251.

Tauro, F., Piscopia, R., & Grimaldi, S. (2019). Ptv-stream: A simplified particle tracking velocimetry framework for stream surface flow monitoring. *Catena*, *172*, 378–386.

Taylor, G. I. (1921). Diffusion by continuous movements. *Proceedings of the London Mathematical Society*, *2*(1), 196–212.

Tennekes, H., & Lumley, J. L. (1972). *A first course in turbulence.* MIT press.

Toschi, F., & Bodenschatz, E. (2009). Lagrangian properties of particles in turbulence. *Annual Review of Fluid Mechanics*, *41*, 375–404.

Turney, D. E., & Banerjee, S. (2013). Air–water gas transfer and near-surface motions. *Journal of Fluid Mechanics*, *733*, 588–624.

Uijttewaal, W., & Booij, R. (2000). Effects of shallowness on the development of free-surface mixing layers. *Physics of Fluids*, *12*(2), 392–402.

Ulseth, A. J., Hall, R. O., Boix Canadell, M., Madinger, H. L., Niayifar, A., & Battin, T. J. (2019). Distinct air–water gas exchange regimes in low-and high-energy streams. *Nature Geoscience*, *12*(4), 259–263.

van Sebille, E., Griffies, S. M., Abernathey, R., Adams, T. P., Berloff, P., Biastoch, A., … Zika, J. D. (2018). Lagrangian ocean analysis: Fundamentals and practices. *Ocean Modelling*, *121*, 49-75.

van den Bremer, T. S., & Breivik, Ø. (2018). Stokes drift. *Philosophical Transactions of the Royal Society A: Mathematical, Physical and Engineering Sciences*, *376*(2111), 20170104.

van Emmerik, T., & Schwarz, A. (2020). Plastic debris in rivers. *Wiley Interdisciplinary Reviews: Water*, *7*(1), e1398.

van Sebille, E., Aliani, S., Law, K. L., Maximenko, N., Alsina, J. M., Bagaev, A., … Wichmann, D. (2020). The physical oceanography of the transport of floating marine debris. *Environmental Research Letters*, *15*(2), 023003.

van Sebille, E., Wilcox, C., Lebreton, L., Maximenko, N., Hardesty, B. D., van Franeker, J. A., … Law, K. L. (2015). A global inventory of small floating plastic debris. *Environmental Research Letters*, *10*(12), 124006.

Vella, D., & Mahadevan, L. (2005). The "cheerios effect". *American Journal of Physics*, *73*(9), 817–825.

Volk, R., Calzavarini, E., Leveque, E., & Pinton, J.-F. (2011). Dynamics of inertial particles in a turbulent von kármán flow. *Journal of Fluid Mechanics*, *668*, 223–235.

Voth, G. A., La Porta, A., Crawford, A. M., Alexander, J., & Bodenschatz, E. (2002). Measurement of particle accelerations in fully developed turbulence. *Journal of Fluid Mechanics*, *469*, 121–160.

Voth, G. A., & Soldati, A. (2017). Anisotropic particles in turbulence. *Annual Review of Fluid Mechanics*, *49*(1), 249–276.

Weitbrecht, V., Kühn, G., & Jirka, G. (2002). Large scale piv-measurements at the surface of shallow water flows. *Flow Measurement and Instrumentation*, *13*(5-6), 237–245.

Zambianchi, E., Iermano, I., Suaria, G., & Aliani, S. (2014). Marine litter in the mediterranean sea: an oceanographic perspective. In *Marine litter in the mediterranean and black seas ciesm workshop monograph* (pp. 31–41).

Zhang, C., Shen, L., & Yue, D. K. (1999). The mechanism of vortex connection at a free surface. *Journal of Fluid Mechanics*, *384*, 207–241.